PNAS

Supporting Information for

Thermodynamic modulation of gephyrin condensation by inhibitory synapse components

Gyehyun Lee, Seungjoon Kim, Da-Eun Hwang, Yu-Gon Eom, Gyubin Jang, Hye Yoon Park, Jeong-Mo Choi, Jaewon Ko, and Yongdae Shin

*Correspondence to Y.S. (ydshin@snu.ac.kr), J.K. (jaewonko@dgist.ac.kr), J.M.C (jmchoi@pusan.ac.kr)

This PDF file includes:

Other supporting materials for this manuscript include the following:

MATERIALS and METHODS

Cell culture. HEK293T (Takara, 632180) cells were cultured in 10% FBS (HyClone, SV30207.02) DMEM (Sigma-Aldrich, D6429) supplemented with penicillin/streptomycin antibiotics (Gibco, 15140122) at 37 °C with 5% CO_2 in a humidified incubator.

Plasmid construction. pEGFP-gephyrin WT was previously described[1]. All assembly reactions of DNA fragments, unless otherwise noted, were performed using HiFi DNA Assembly Kit (NEB, E2621S). To generate IDR-mCh-Cry2 constructs, DNA fragments were amplified by PCR using HiFi PCR premix (Takara, 639298) and assembled into the pHR lentiviral backbone with Cry2PHR (Addgene #101221). cDNA clones encoding human FUS, DDX4, G3BP1, were obtained from Korea Human Gene Bank (Medical Genomics Research Center, Korea). G-E, G-C_i-E, ΔC_4, G-IDR-E constructs were generated from pEGFP-gephyrin WT through the linearizing PCR of backbone followed by reassembly with corresponding PCR-amplified DNA fragments. Gephyrin variants of KR/DE4, KR/DE8, G-FUS_{IDR}(GS/KR8)-E and Charge-flipped-E domain (E435K, D437R, D438R, E441K, E442K, E444K) were generated using Q5 Site-Directed Mutagenesis Kit (NEB, E0554S). To generate mCh-labeled iPSD components, DNA fragments for GlyR-β (residues 349-474), $GABA_AR$-α3 (residues 360-460) and GCN4 were synthesized (BIONICS). IQSEC3 DNA fragment was amplified from FLAG-IQSEC3[2]. These fragments were assembled into the C2 backbone deprived from pEGFP-gephyrin WT. $NLGN2_{cy}$ (residues 699-836) was synthesized (BIONICS) and assembled into the pHR lentiviral backbone to generate $NLGN2_{cy}$-mCh-Cry2 $NLGN2_{cy}$-FUS_N-mCh-Cry2, myr-mCh-Cry2-$NLGN2_{cy}$ constructs. The resulting constructs were fully sequenced to confirm the absence of unwanted substitutions.

Hippocampal neuron culture. Dissociated mouse hippocampal neurons were prepared as previously described[3]. Briefly, hippocampi were dissected from the brains of 0.5- to 2-day-old mouse pups (C57BL/6 background) and dissociated with trypsin. The dissociated neurons were seeded at a concentration of 420,000 cells/mL on a confocal dish (Cellvis, D35-20-1) coated with poly-D-lysine (Sigma-Aldrich, P7886) and incubated at 37˚C with 5% CO_2 for about 4 hours to enable them to adhere to the bottom of the dish. The neurons were then incubated with B-27 supplement (Gibco, 17504044), GlutaMax supplement (Gibco, 35050061), 0.1 mg/mL Primocin (InvivoGen, ant-pm-1) in Neurobasal-A medium (Gibco, 10888022). Rat hippocampal neurons were prepared from E18 rat brains cultured on coverslips coated with poly-L-lysine, and grown in Neurobasal medium supplemented with B-27 (Invitrogen), 0.5% FBS, 0.5 mM GlutaMax (Invitrogen), and sodium pyruvate (Invitrogen), as previously described[4]. The experiments involving animals were carried out in accordance with the Institutional Animal Care and Use Committee of Seoul National University and DGIST.

Antibodies. The following antibodies were commercially purchased: goat polyclonal anti-EGFP (Rockland; RRID: AB_218182), rabbit polyclonal anti-$GABA_AR$γ2 (Synaptic Systems; RRID: AB_2263066), and mouse polyclonal anti-VGAT (Synaptic Systems; RRID: AB_887872).

Cell transfections. For HEK293T cells, cells were transfected using Lipofectamine 3000 transfection reagent (Invitrogen, L3000015). For mouse and rat hippocampal neurons, cells were transfected using Lipofectamine 3000 and CalPhos Kit (Clontech), respectively, at DIV10.

Live cell imaging. HEK293T cells were plated on the TC treated confocal dish (SPL, 100350) and grown in regular growth medium to reach ~80% confluency. Mouse hippocampal neurons pre-cultured on the confocal dish (Cellvis, D35-20-1) were transfected a day prior to imaging. Live cell imaging was performed using a Nikon 60X oil immersion objective (NA 1.4; Nikon, MXA22168) on a Nikon A1 laser scanning confocal microscope equipped with a CO_2 microscope stage incubator under 5% CO_2 and 37˚C. For global activation, cells were imaged using two laser lines (488-nm for Cry2 activation, 560-nm for mCherry imaging).

Fluorescence recovery after photobleaching (FRAP) assay. HEK293T were plated on the TC treated confocal dish, and a day after transfected with EGFP-gephyrin. Nikon A1 confocal microscope with Nikon 60X oil immersion objective (NA 1.4; Nikon, MXA22168) was used to perform FRAP experiments. After taking 6 initial images, the selected region was bleached using 488-nm laser, followed by acquisition of 60 images every 5 sec. To create fluorescence recovery curves, fluorescence intensities were normalized with the average intensities of the initial images.

Quantification of saturation concentrations of gephyrin variants. All quantification was performed using ImageJ software. To characterize the saturation concentration of gephyrin variants, we first identified the presence of condensates in individual cell images. Then, cytoplasmic intensities of gephyrin variants were measured from areas devoid of condensates. For comparison, all experiments for the characterization of saturation concentrations were conducted using the same imaging conditions.

Quantification of condensate intensity in HEK293T cells. Fluorescence intensities within condensates were measured for the construction of ternary phase diagrams and the examination of condensate maturation. For these measurements, cells were z-stack imaged with 0.5 μm intervals (Total 5 μm). To prevent underestimation of fluorescence intensities associated with diffraction limits, we used only those condensates of which radius were bigger than 0.75 μm and showing similar intensity levels over at least three z-stack sections. Condensate boundaries were identified in the maximum-projection images using the Otsu threshold algorithm. The interface of identified condensates exhibited a gradual increase in fluorescence intensity due to the optical resolution limit, and thus the mean values of pixels top 10 percent in intensity were taken as dense-phase concentration for individual condensates. Quantification was performed using ImageJ software.

Replica Exchange Monte Carlo protein simulations. The atomistic Monte Carlo (MC) simulations were conducted using the CAMPARI v4 package[5], employing the ABSINTH implicit solvation model and forcefield paradigm[6,7]. We performed atomistic Monte Carlo simulations on three systems: the wildtype, KR/DE4, and KR/DE8 gephyrin dimer systems. Each system consisted of the C and E domains of chain A and the E domain of chain B. The simulations were conducted under the spherical soft-wall boundary condition with a radius of 400 Å. To generate the initial structures, the folded E domain was obtained from PDB 2FU3, while the disordered C domains were generated *de novo* using CAMPARI. To maintain the conformational stability of the E domain, we applied constraints on the internal degrees of freedom of residues within the folded region, specifically residues 323 to 736, which spans the entire E domain and a portion of the C domain. Each simulation was comprised of 1.5×10^7 MC steps, with a sampling frequency of $(5{,}000 \text{ steps})^{-1}$, resulting in 3,000 data points per simulation. To ensure adequate sampling, we

employed 14 replicas for each system, following the temperature schedules utilized in previous studies[8,9]. The temperature schedules were as follows: 300K, 306K, 313K, 320K, 330K, 340K, 350K, 360K, 375K, 390K, 405K, 420K, 435K, and 450K. Replica exchange attempts were made every 2,000 steps.

Generation of contact frequency maps from simulation results. Two residues are considered to be in contact if the minimum distance between any arbitrary pair of atoms from the two residues is smaller than 5 Å. The number of frames where the two residues are in contact was normalized by the total number of frames to obtain the contact frequency for each residue-residue pair. To improve readability of pairwise contract frequency maps, filtered contact-frequency differences were generated by convoluting raw data with a Gaussian kernel with a variance of 4 pixels and a radial size of 8 pixels. The convolution and contour mapping were performed using custom-built MATLAB scripts.

Immunocytochemistry. Rat hippocampal neurons were immunostained at DIV14. Transfected cultured neurons were fixed with 4% paraformaldehyde/4% sucrose, permeabilized with 0.2% Triton X-100 in PBS, immunostained with primary antibodies as indicated, and detected with the indicated secondary antibodies. For immunostaining experiments, the following primary antibodies were used: anti-EGFP (1:500), anti-VGAT (1: 500), and anti-$GABA_AR\gamma2$ (1: 500). The following secondary antibodies were also used: FITC-conjugated donkey anti-goat (Jackson ImmunoResearch; RRID: AB_631727) Cy3-conjugated donkey anti-rabbit (Jackson ImmunoResearch; RRID: AB_2307443), and anti-mouse Alexa Fluor™ 647 (Thermo Fisher Scientific; RRID: AB_2896356).

Rat hippocampal neuron image acquisition. For rat hippocampal neurons, images were acquired using a confocal microscope (LSM800, Carl Zeiss) with a 63x objective lenses. Z-stack images were converted to maximal projection and analyzed to obtain the density and size of puncta immunoreactivities of marker proteins.

Quantification of puncta density and synaptic targeting in cultured rat hippocampal neurons. Quantification was performed in a blinded manner using MetaMorph software (Molecular Devices Corp.). For quantification of GABAergic synaptic targeting of EGFP-gephyrin variants, overlaying red ($GABA_AR\gamma2$) and magenta (VGAT) color images were separately obtained using the color threshold function in ImageJ (NIH). Regions of interests (ROIs) from distal dendrites were defined according to EGFP fluorescence. The degree of colocalization of green (i.e., EGFP fluorescence) and overlaid red ($GABA_AR\gamma2$)/magenta (VGAT) in the ROIs was calculated using the colocalization module in MetaMorph.

Electrophysiology. Cultured hippocampal neurons were transfected with pEGFP-gephyrin WT or the indicated variants at DIV10, followed by whole-cell patch clamp recordings at DIV14–16, as previously described[10]. Glass Pipettes were pulled from borosilicate glass (o.d. 1.5 mm, i.d. 0.86 mm; Sutter Instrument) using a Model P-97 pipette puller (Sutter Instrument). The internal solution consisted of 145 mM CsCl, 5 mM NaCl, 10 mM HEPES, 10 mM EGTA, 0.3 mM Na-GTP, and 4 mM Mg-ATP. The internal solution pH was set 7.2–7.4 with CsOH, and an osmolarity of 290–295 mOsmol/L. The external solution consisted of 130 mM NaCl, 4 mM KCl, 2 mM $CaCl_2$, 1 mM $MgCl_2$, 10 mM HEPES, and 10 mM D-glucose with pH adjusted to 7.2–7.4 with NaOH, and an osmolarity

of 300–305 mOsmol/L. For mIPSC recordings, external solution was treated with 1 mM TTX, 10 mM CNQX and 50 mM AP-5 to block Na^+ currents, AMPARs and NMDARs, respectively. Pipettes were filled with internal solution, resistance was 3–6 MΩ. Instrument of whole cell recording consists of MPC-200 manipulators (Sutter Instrument) and a Multiclamp 700B amplifier (Molecular Devices) in -70 mV of holding potential condition. Synaptic currents were analyzed offline using Clampfit 10.8 (Molecular Devices) software.

Polyphasic linkage model. In general, the preferential binding of ligands to one of two phases A and B of scaffolds, corresponding to dilute and condensate phases in this work, respectively, results in the change of the saturation concentration of scaffold as follows[11]:

$$c_{\mathrm{sat}} = c_{\mathrm{sat}}^{\mathrm{o}} \frac{1 + K_{\mathrm{A1}}[\mathrm{L}] + K_{\mathrm{A2}}[\mathrm{L}]^2 + K_{\mathrm{A3}}[\mathrm{L}]^3 + \cdots}{1 + K_{\mathrm{B1}}[\mathrm{L}] + K_{\mathrm{B2}}[\mathrm{L}]^2 + K_{\mathrm{B3}}[\mathrm{L}]^3 + \cdots},$$

where $c_{\mathrm{sat}}^{\mathrm{o}}$ is the client-free saturation concentration, $[\mathrm{L}]$ is the concentration of free clients, and K_{ij} denotes the association constant for the reaction $j\mathrm{L} + \mathrm{S}^{(i)} \rightleftarrows \mathrm{SL}_j^{(i)}$ between client L and scaffold S in phase i. For simplicity, we assume first-order binding polynomials, which leads to

$$c_{\mathrm{sat}} = c_{\mathrm{sat}}^{\mathrm{o}} \frac{1 + K_{\mathrm{A1}}[\mathrm{L}]}{1 + K_{\mathrm{B1}}[\mathrm{L}]}.$$

We combined this model with other thermodynamic equations, including mass conservation and the lever rule, to yield the following five equations (Fig. 6f):

- Total client concentration: $[\mathrm{L}]_{\mathrm{T}} = [\mathrm{L}] + K_{\mathrm{A}}[\mathrm{L}][\mathrm{S}]_{\mathrm{A}} + K_{\mathrm{B}}[\mathrm{L}][\mathrm{S}]_{\mathrm{B}}$
- Total scaffold concentration (lever rule): $[\mathrm{S}]_{\mathrm{T}} = c_{\mathrm{A}}\phi_{\mathrm{A}} + c_{\mathrm{B}}(1 - \phi_{\mathrm{A}})$
- Total dilute-phase scaffold concentration: $[\mathrm{S}]_{\mathrm{A}}(1 + K_{\mathrm{A}}[\mathrm{L}]) = c_{\mathrm{A}}\phi_{\mathrm{A}}$
- Total dense-phase scaffold concentration: $[\mathrm{S}]_{\mathrm{B}}(1 + K_{\mathrm{B}}[\mathrm{L}]) = c_{\mathrm{B}}(1 - \phi_{\mathrm{A}})$
- Dilute-phase arm: $c_{\mathrm{A}} = c_{\mathrm{A}}^{\mathrm{o}}(1 + K_{\mathrm{A}}[\mathrm{L}])/(1 + K_{\mathrm{B}}[\mathrm{L}])$

Here, we have five unknown variables:

- Volume fraction of the dilute phase ϕ_{A}
- Concentration of free client $[\mathrm{L}]$
- Concentration of free dilute-phase scaffolds $[\mathrm{S}]_{\mathrm{A}}$
- Concentration of free dense-phase scaffolds $[\mathrm{S}]_{\mathrm{B}}$
- Dilute-phase arm c_{A}

As we have five equations and five variables, we can numerically solve the equations to determine the variables, if the following constants are given:

- Total client concentration $[\mathrm{L}]_{\mathrm{T}}$
- Total scaffold concentration $[\mathrm{S}]_{\mathrm{T}}$

- Association constants K_{A} and K_{B}
- Dilute-phase arm with no client $c_{\mathrm{A}}^{\mathrm{o}}$
- Dense-phase arm (assumed to be constant) $c_{\mathrm{B}} = c_{\mathrm{B}}^{\mathrm{o}}$

c_{B} is assumed to be constant as indicated by experimental data. To numerically construct ternary phase diagrams, the value of 1 μM was assumed for $c_{\mathrm{A}}^{\mathrm{o}}$, and $c_{\mathrm{B}}^{\mathrm{o}}$ was set to be consistent with the experimentally measured ratio of scaffold concentrations in the dense phase to the dilute one (Fig. 6d). We numerically solved our system of equations for various combinations of the remaining four constants, to examine the effects of different association constants and total concentrations on ternary phase diagrams (Fig. 6g).

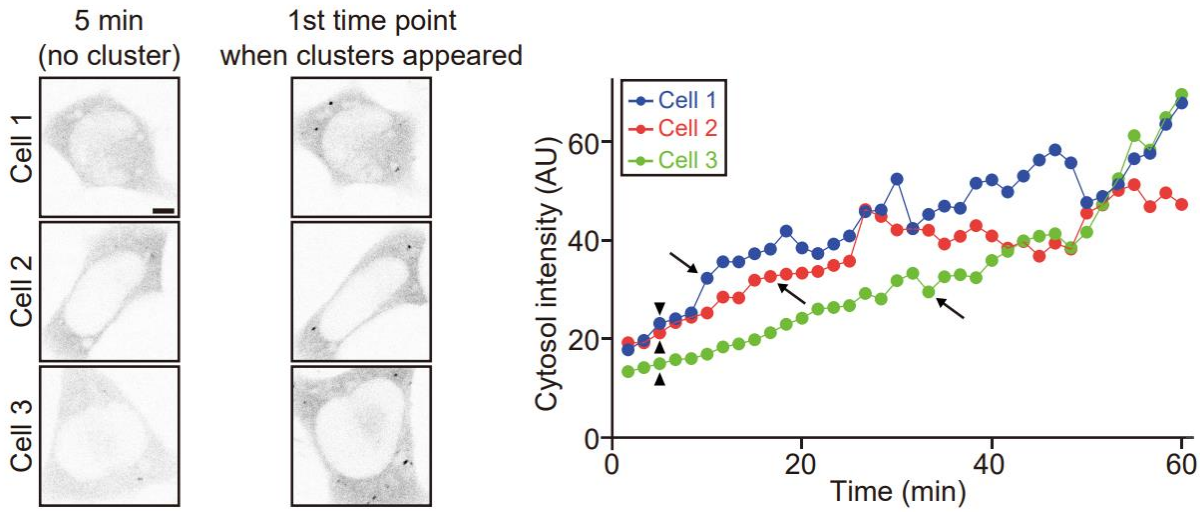

Supplemental Figure 1. **Gephyrin cluster formation analysis**
(Left) Fluorescence images of EGFP tagged gephyrin in HEK293T cells, before and after cluster formation. Scale bar, 6 μm. (Right) Temporal evolutions of cytosolic fluorescence for cells. Arrows indicate the first time point at which gephyrin clusters are observed. Arrowheads indicate 5-min time points at which condensates are not observed.

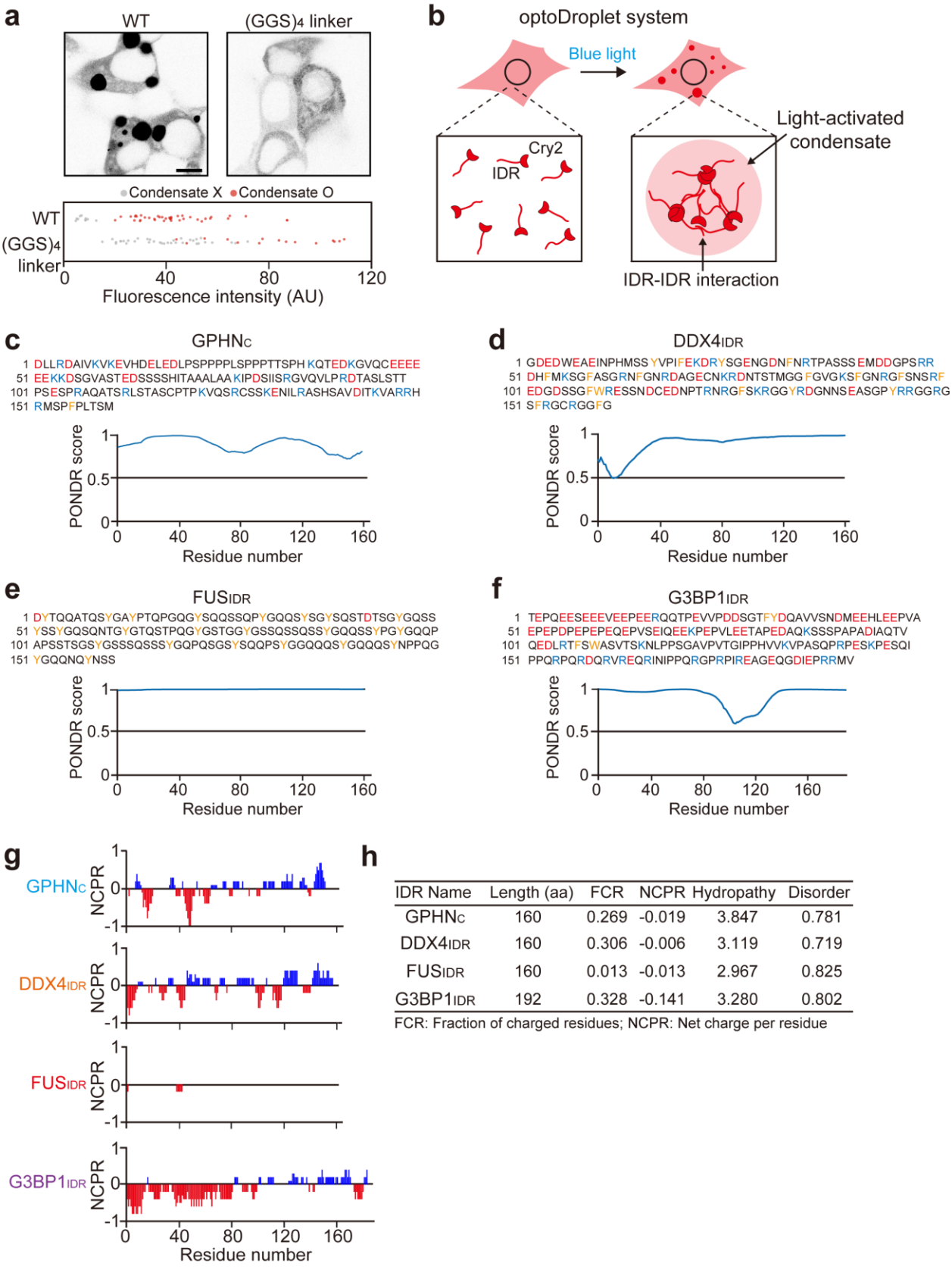

IDR Name	Length (aa)	FCR	NCPR	Hydropathy	Disorder
GPHNC	160	0.269	-0.019	3.847	0.781
DDX4IDR	160	0.306	-0.006	3.119	0.719
FUSIDR	160	0.013	-0.013	2.967	0.825
G3BP1IDR	192	0.328	-0.141	3.280	0.802

FCR: Fraction of charged residues; NCPR: Net charge per residue

Supplementary Figure 2. The effect of the central IDR linker on gephyrin condensation
a (Top) Fluorescence images of EGFP-tagged gephyrin WT and a variant of which the C domain is replaced with $(GGS)_4$ linker. Scale bar, 8 μm. (Bottom) Cytosolic fluorescence intensities of HEK293T cells expressing gephyrin WT or the variant. n = 50 for both constructs.
b Schematic of the optoDroplet system. optoDroplet constructs consist of the N-terminal IDR fused to mCh fluorescent protein and the Cry2PHR domain.
c-f Amino acid sequences (blue = positively charged, red = negatively charged, yellow = aromatic) and IDR predictions of various IDR linkers used in this study.
g Net charge per residue of the IDR linkers, calculated with a sliding window of 5 residues.
h Properties of amino acid sequences of the IDR linkers.

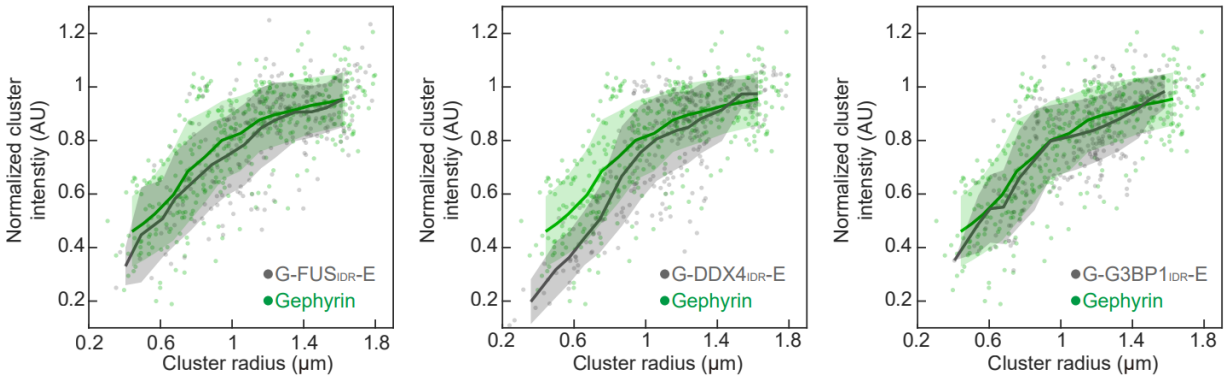

Supplemental Figure 3. Maturation behaviors of gephyrin linker variants

Fluorescence intensities of G-FUS$_{IDR}$-E (Left), G-DDX4$_{IDR}$-E (Middle), and G-G3BP1$_{IDR}$-E (Right) clusters, together with WT gephyrin clusters, are plotted against cluster radius. Data are normalized with maximum values of individual cells. Clusters at several time points were measured from multiple cells for each sample type. Solid lines and shaded areas indicate the average and standard deviation of data points located within 0.3 μm window. G-FUS$_{IDR}$-E, n = 251 (10 cells); G-DDX4$_{IDR}$-E, n = 277 (10 cells); G-G3BP1$_{IDR}$-E, n = 262 (10 cells); Gephyrin, n = 410 (16 cells).

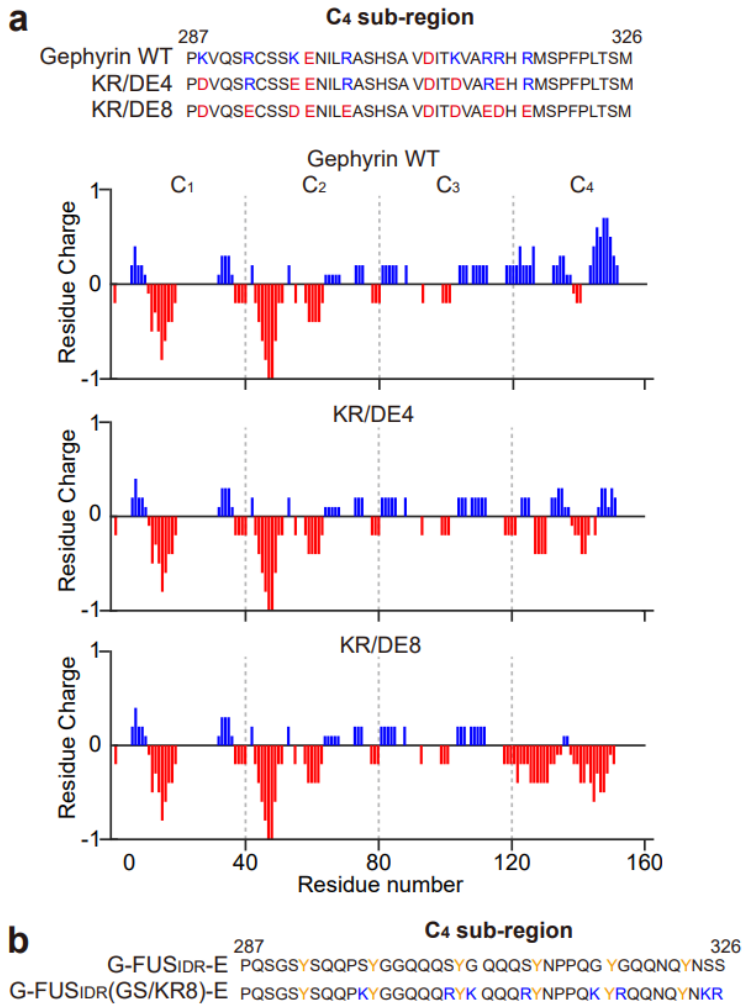

Supplementary Figure 4. The role of positively charged residues in the C domain on gephyrin condensation

a (Top) Amino acid sequence of gephyrin variants, KR/DE4 and KR/DE8 (blue, positively charged; red, negatively charged). (Bottom) Net charge per residue of gephyrin WT or variants, calculated with a sliding window of 5 residues.

b Amino acid sequence of G-FUS$_{IDR}$-E and G-FUS$_{IDR}$(GS/KR8)-E constructs (blue, positively charged; yellow, aromatic).

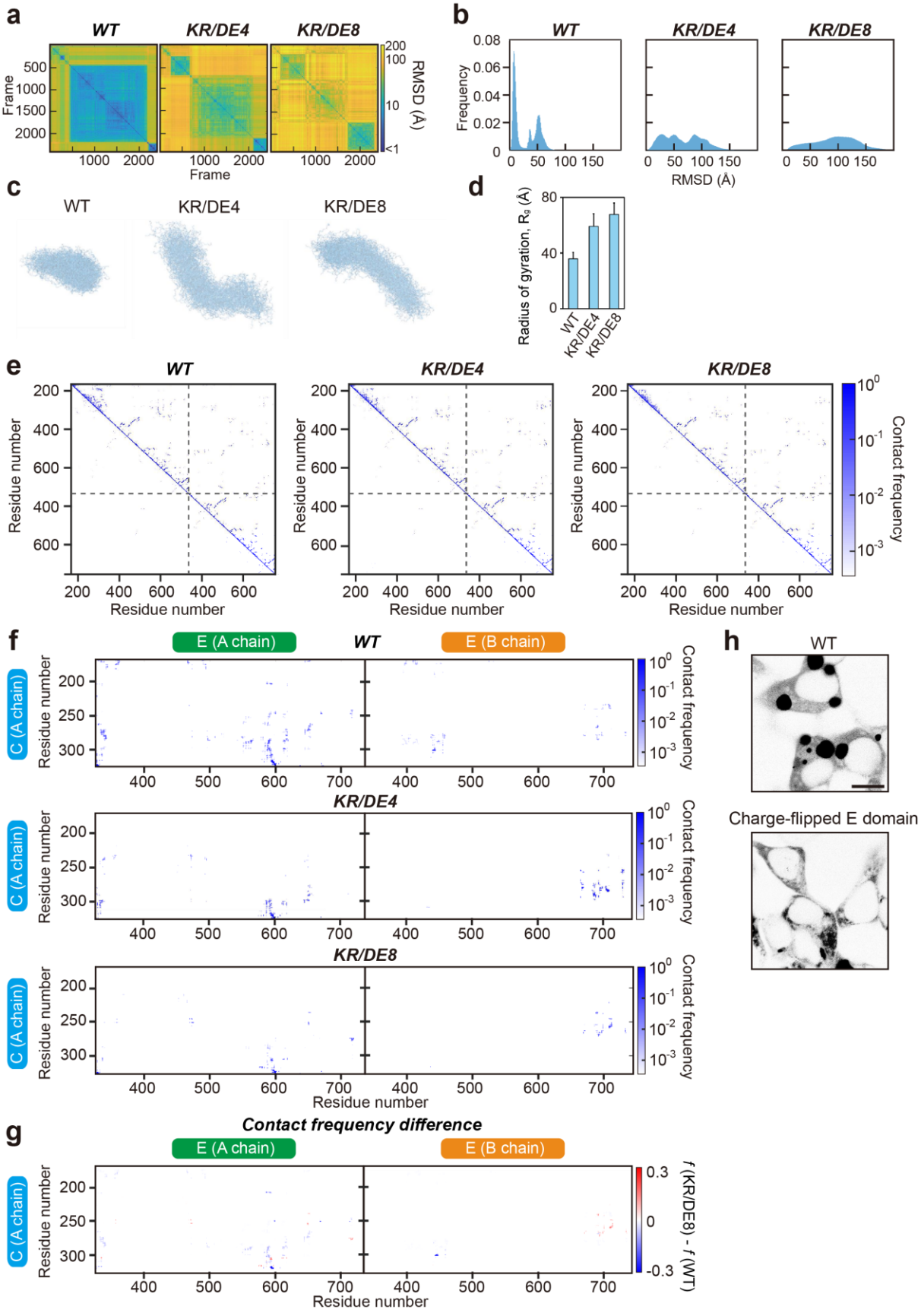
a
WT
KR/DE4
KR/DE8
Frame
RMSD (Å)
b
Frequency
RMSD (Å)
c
d
Radius of gyration, R_g (Å)
e
Residue number
Contact frequency
f
E (A chain)
E (B chain)
C (A chain)
g
Contact frequency difference
f (KR/DE8) - f (WT)
h
WT
Charge-flipped E domain

Supplementary Figure 5. Atomistic simulations of gephyrin domain interactions
a Frame-to-frame RMSD data from atomistic Monte Carlo simulations of the (left) gephyrin WT, (middle) KR/DE4, and (right) KR/DE8 variants. Each pixel represents the RMSD value between two simulation frames. The order of frames has been rearranged to show the checkerboard patterns clearly. WT shows well-defined similar structures ("clusters" in structural ensemble), which are not dramatic in the case of the other two systems.
b Frequency histograms for the distributions of the RMSD values (panel **a**), obtained from the simulations of the (left) WT, (middle) KR/DE4, and (right) KR/DE8 gephyrin systems. WT structures show the closest similarities; a peak around the RMSD value of 10 Å can be regarded as the group of the structure belonging to the same cluster in the ensemble. The two variant systems show significantly weaker patterns.
c Structure ensembles of the C domain in isolation. The C domains of gephyrin WT, KR/DE4, and KR/DE8 mutants are used in atomistic Monte Carlo simulations.
d Radii of gyration of the C domain in isolation. Error bars, ±SD; WT, 35.9 ± 4.7 Å; KR/DE4, 59.3 ± 9.1 Å; KR/DE8, 67.8 ± 8.2 Å.
e Contact frequency data for the (left) WT, (middle) KR/DE4, and (right) KR/DE8 gephyrin systems. To remove the redundancy, we utilize only the upper trigonal part of the contact map.
f Contact frequency data for the interactions between the C and E domains of the (top) WT, (center) KR/DE4, and (bottom) KR/DE8 gephyrin systems. The corresponding regions from the contact frequency data (panel **e**) are enlarged for clarity.
g Contact frequency difference data between the WT and KR/DE8 gephyrin systems. The interactions between the C and E domains are only shown.
h Fluorescence images of gephyrin WT or a variant with E domain charge flipped. The charge-flipped domain contains six DE-to-KR mutations in the E domain. Scale bar, 8 μm.

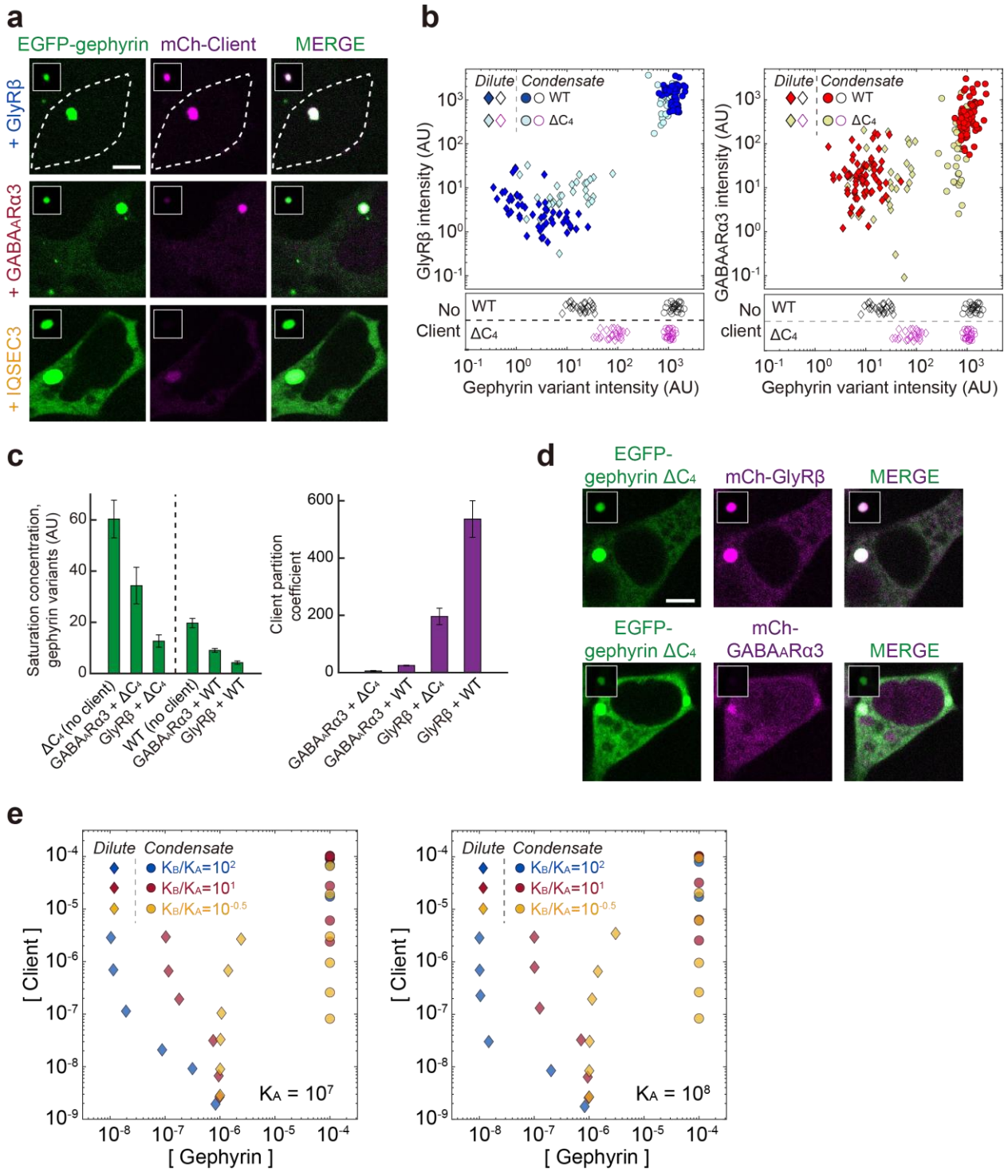

Supplementary Figure 6. Ternary phase diagram of gephyrin ΔC$_4$ and clients
a Fluorescence images of HEK293T cells co-expressing EGFP-tagged gephyrin and mCh-tagged iPSD components. Gephyrin and iPSD component expression levels are similar across these cells. For comparison, images are shown at the same brightness level. White dotted lines indicate cell boundary. Insets display gephyrin condensates in individual cells. Note that different brightness levels are used between the whole-cell images and insets. Scale bars, 6 μm.

b Ternary phase diagram of the gephyrin variant ΔC_4 with either GlyRβ (left) or $GABA_AR\alpha3$ (right). For comparison, dilute- and dense-phase boundaries in the absence of any client are shown at the bottom. GlyRβ + gephyrin WT, n = 52; GlyRβ + gephyrin ΔC_4, n = 30; $GABA_AR\alpha3$ + gephyrin WT, n = 73; $GABA_AR\alpha3$ + gephyrin ΔC_4, n = 30; gephyrin WT and ΔC_4 no client, n = 25.
c Saturation concentration of gephyrin variants in the presence or absence of specific iPSD components (left). Partition coefficients of iPSD components, defined as a ratio of the concentration inside gephyrin condensates versus the surrounding cytoplasm (right). Cells with similar expression levels are used in these quantifications. Error bars, ± SEM; gephyrin WT alone, n = 17; ΔC_4 alone, n = 7; GlyRβ + gephyrin WT, n = 37; GlyRβ + gephyrin ΔC_4, n = 21; $GABA_AR\alpha3$ + gephyrin WT, n = 42; $GABA_AR\alpha3$ + gephyrin ΔC_4, n = 11.
d Fluorescence images of HEK293T cells co-expressing EGFP-tagged gephyrin ΔC_4 and mCh-tagged iPSD components. Gephyrin and iPSD component expression levels are similar across these cells. For comparison, images are shown at the same brightness level. Insets display gephyrin condensates in individual cells. Note that different brightness levels are used between the whole-cell images and insets. Scale bars, 6 μm.
e Predicted ternary phase diagrams based on the polyphasic linkage model ($K_A=10^7$, 10^8 M^{-1}). To generate the diagrams, six different pairs of total gephyrin/client concentrations are used for each condition. All concentrations are in molarity.

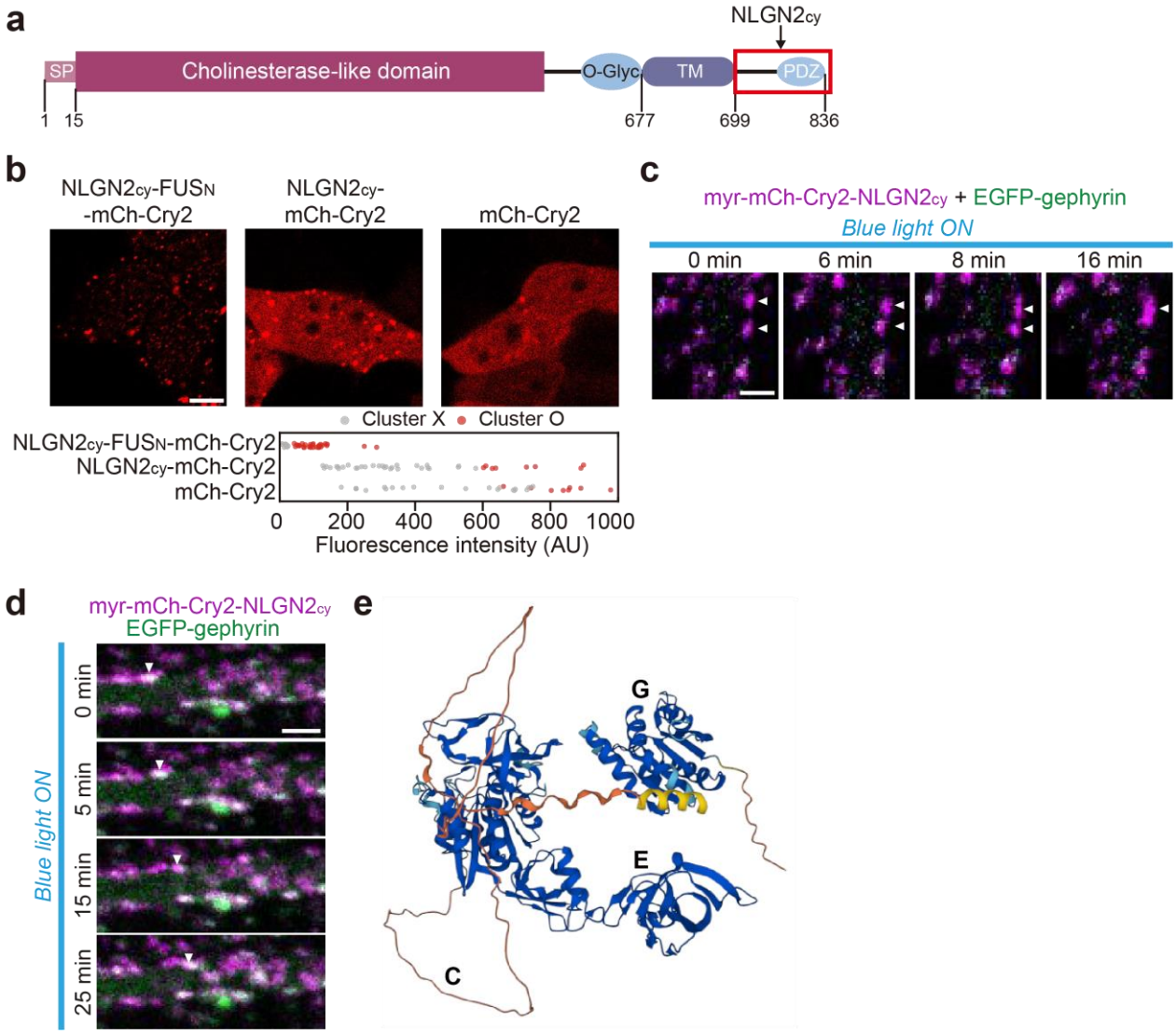

Supplementary Figure 7. The NLGN2-mediated regulation of gephyrin condensation
a The domain architecture of NLGN2.
b (Top) Fluorescence images of the HEK293T cells expressing optoDroplet constructs with different fusions. All cells are activated under identical blue-light conditions. Scale bar, 6 μm. (Bottom) Cytosolic fluorescence intensities of HEK293T cells expressing optoDroplet variants.
c-d Time-lapse fluorescence images of the cultured mouse hippocampal neuron expressing EGFP-tagged gephyrin and myr-mCh-Cry2-NLGN2$_{cy}$ after blue-light activation. White arrowheads indicate membrane-tethered NLGN2$_{cy}$ optoDroplet clusters exhibiting lateral movements. Scale bar, 1 μm (c) and 2 μm (d).
e Three-dimensional structure of gephyrin predicted from Alphafold (code: Q9NQX3).

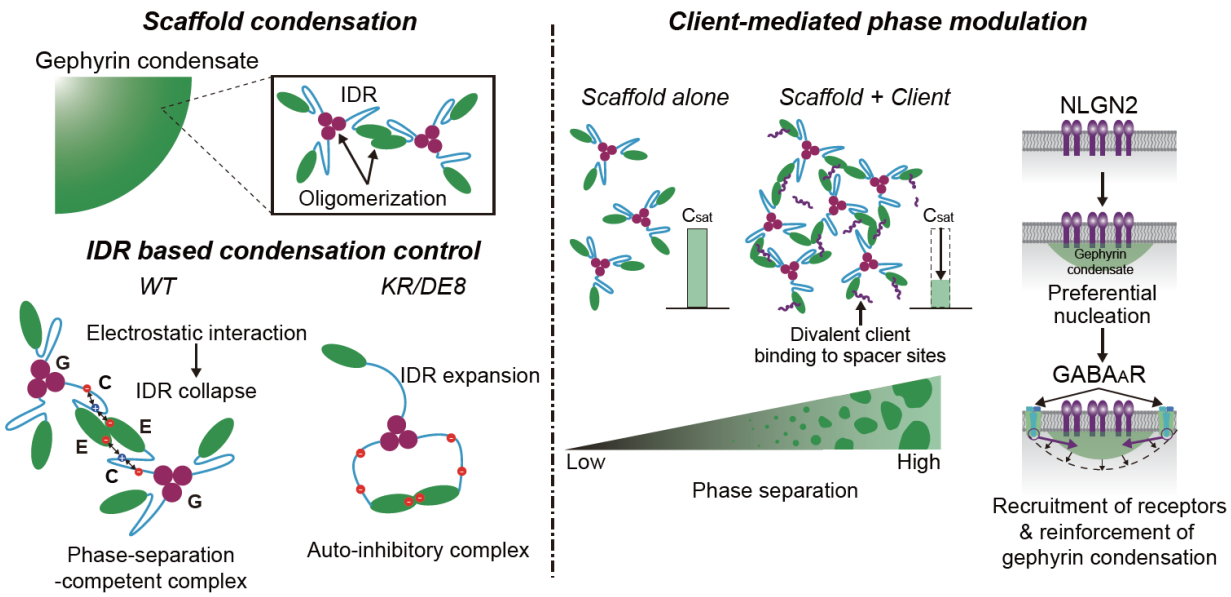

Supplementary Figure 8. Modulation of gephyrin phase separation through intra and inter-molecular interactions

(Top left) Gephyrin condensation is driven by the oligomerization of G and E domain. (Bottom left) The central IDR linker, gephyrin C domain, critically modulates phase separation. The positively charged residues at the C-terminal end of C domain promote gephyrin condensation through intra- and inter-domain interactions. Collectively, these interactions centered around C domain may facilitate the dimerization of E domains from separate trimeric complexes of gephyrin, thereby enhancing phase separation. In contrast, the dimerization of E domains within the single trimer unit can generate the auto-inhibitory form incompetent for phase separation. (Right) Other iPSD components thermodynamically modulate phase separation of gephyrin. Neurotransmitter receptors provide extra physical crosslinks between gephyrin molecules and lower the threshold concentration for phase separation. Local enrichment of gephyrin binding factors such as NLGN2 can lead to preferential nucleation of gephyrin condensates which then recruit other iPSD components for further phase modulation.

Movie S1. The atomistic Monte Carlo simulation of gephyrin with the WT C domain.
Movie S2. The atomistic Monte Carlo simulation of gephyrin with the C domain charge mutant KR/DE4.
Movie S3. The atomistic Monte Carlo simulation of gephyrin with the C domain charge mutant KR/DE8.

SI References

1. Kim, S. *et al.* Impaired formation of high-order gephyrin oligomers underlies gephyrin dysfunction-associated pathologies. *iScience* **24**, 102037 (2021).
2. Um, J. W. *et al.* IQ Motif and SEC7 domain-containing protein 3 (IQSEC3) interacts with gephyrin to promote inhibitory synapse formation. *J. Biol. Chem.* **291**, 10119–10130 (2016).
3. Song, M. S., Moon, H. C., Jeon, J.-H. & Park, H. Y. Neuronal messenger ribonucleoprotein transport follows an aging Levy walk. *Nat. Commun.* **9**, 344 (2018).
4. Um, J. W., Han, K. A., Choi, S. Y. & Ko, J. Protocol for Quantitative Analysis of Synaptic Vesicle Clustering in Axons of Cultured Neurons. *STAR Protoc.* **1**, 100095 (2020).
5. Vitalis, A. & Pappu, R. V. Methods for Monte Carlo Simulations of Biomacromolecules. *Annu. Rep. Comput. Chem.* **5**, 49–76 (2009).
6. Vitalis, A. & Pappu, R. V. ABSINTH : A New Continuum Solvation Model for Simulations of Polypeptides in Aqueous Solutions. *J. Comput. Chem.* **30**, 673–699 (2008).
7. Choi, J.-M. & Pappu, R. V. Improvements to the ABSINTH Force Field for Proteins Based on Experimentally Derived Amino Acid Specific Backbone Conformational Statistics. *J. Chem. Theory Comput.* **15**, 1367–1382 (2019).
8. Das, R. K., Crick, S. L. & Pappu, R. V. N-terminal segments modulate the α-helical propensities of the intrinsically disordered basic regions of bZIP proteins. *J. Mol. Biol.* **416**, 287–299 (2012).
9. Das, R. K. & Pappu, R. V. Conformations of intrinsically disordered proteins are influenced by linear sequence distributions of oppositely charged residues. *Proc Natl Acad Sci USA* **110**, 13392–13397 (2013).
10. Han, K. A. *et al.* PTPσ Controls Presynaptic Organization of Neurotransmitter Release Machinery at Excitatory Synapses. *iScience* **23**, 101203 (2020).
11. Wyman, J. & Gill, S. J. Ligand-linked phase changes in a biological system: Applications to sickle cell hemoglobin. *Proc. Natl. Acad. Sci. U. S. A.* **77**, 5239–5242 (1980).